The University of Osaka
Institutional Knowledge Archive

Title	Non-contact imaging of subsurface defects using a scanning laser source
Author(s)	Hayashi, Takahiro; Mori, Naoki; Ueno, Tomotake
Citation	Ultrasonics. 2021, 119, p. 106560
Version Type	AM
URL	https://hdl.handle.net/11094/85206
rights	© 2021 Published by Elsevier B.V. This manuscript version is made available under the Creative Commons Attribution-NonCommercial-NoDerivatives 4.0 International License.
Note	

The University of Osaka Institutional Knowledge Archive : OUKA

https://ir.library.osaka-u.ac.jp/

The University of Osaka

Highlights

Subsurface defects are visualized using a scanning laser source.
The defect images are significantly affected by local defect resonant frequency.
This imaging technique is useful for in-situ testing of additive manufacturing.

Non-contact imaging of subsurface defects using a scanning laser source

Takahiro Hayashi[a], Naoki Mori[a], and Tomotake Ueno[a]
[a] Department of Mechanical Engineering, Graduate School of Engineering,
Osaka University, Suita, Osaka 565-0871, Japan

Abstract

The quality of additive manufacturing (AM) components must be guaranteed to ensure wide applicability, and a nondestructive inspection technology is required in this regard. Therefore, this study examined a method for detecting subsurface defects using ultrasonic waves excited by a laser. Fundamental experiments showed that wideband ultrasonic waves can be excited with a suitable signal-to-noise ratio using high-repetition laser pulses. Images of subsurface defects were appropriately obtained using a scanning laser source (SLS) with broadband waves for an aluminum alloy flat plate with artificial defects. The imaging experiments showed that the acquisition condition depends on the local defect resonant (LDR) frequency in the defective part. The imaging technique also enabled to detect subsurface circular defects created by AM with the diameter below 1.0 mm that were undetectably small in our previous study using the SLS. Based on results of these experiments and a finite element analysis, the following guideline is proposed: the LDR frequencies of targeted defects must be included in the tested frequency range.

Keywords: laser ultrasonics; defect imaging; scanning laser source; subsurface defects

1. Introduction

Components manufactured via additive manufacturing (AM) can easily be used to create complex shapes that cannot be realized via conventional subtraction processing and welding assembly techniques. For obtaining lightweight and highly functional structures, AM components have been widely used even in primary structures, in which catastrophic failure could occur if the components are defective. However, in AM, powders and wires are stacked and hardened; thus, voids, cracks, delamination, and insufficient fusion may occur because of the modeling principle, which may cause a decrease in the strength of the structure. Therefore, non-destructive inspection, which guarantees the quality of the components, is a very important technology for expanding the use of AM parts [1–10].

Non-destructive inspection to guarantee the quality of AM components can be classified into offline inspection after manufacturing and in-situ monitoring performed during manufacturing. Regarding offline inspection, research on applying conventional non-destructive inspections to AM components has been widely attempted, and X-ray computed tomography (X-ray CT) and ultrasonic C-scan techniques have been used to inspect components [1,4]. X-ray CT is a technology that measures transmission X-rays from all directions of an object and reconstructs its transmittance in three dimensions. In recent years, micro-focus X-ray CT, which can detect voids and interventions in the μm order, has been widely used. Although X-ray CT is a highly versatile technology, it cannot be applied in principle to large metal components that cannot easily transmit X-rays.

In the imaging of internal structures via ultrasonic C-scan, the object is submerged in water, and ultrasonic waves propagate to the object through water. At this time, an echo from the internal void and inclusion is generated by the acoustic impedance difference between water and the internal defects, and the corresponding images can be acquired by scanning the ultrasonic transducer. However, the acoustic impedance difference between water and the object is also often large, and in the case of complex structures, such as those shaped via AM, a large number of echo signals from the water–component interface appear, and it becomes difficult to evaluate the internal structure of the component. Simonetti et al. developed a new technique called cryo-ultrasonic nondestructive evaluation to apply such complex AM components [11]. In this method, by submerging the components in water and freezing them, the acoustic impedance difference between the ice and modeling object is reduced. Laser ultrasonics is also a promising technique as a non-contact ultrasonic inspection and material characterization for AM components. Patel et al. created the texture images of AM components using a surface acoustic waves that generated and detected by laser using spatially resolved acoustic spectroscopy with a speckle knife edge detector [6]. Cerniglia and Montinaro presented the applicability of laser-ultrasonic pulse echo technique to sub-millimeter defects in Inconel samples [7].

Many in-situ monitoring technologies involve observing visible light and temperature images of the AM components from the window of a molding chamber using charge-coupled devices (CCDs) and infrared cameras [2,8–10]. In selective laser melting (SLM), because a CCD camera can be installed on the optical axis of the laser, the melting pool can be thoroughly observed. In the case of in-situ monitoring, feedback on the results can be provided to ensure more precise process control, and the quality of the AM component can be improved. However, once voids and inclusions are incorporated into materials and thus cannot be viewed from the surface, they cannot be found in the camera images.

Accordingly, this study investigates an in-situ imaging technique that can visualize damages near the surface layer using ultrasonic waves generated by laser irradiation. The scanning laser source (SLS) technique can detect damage much smaller than the wavelength without depending on the shape of the object [12–19]. In subsequent sections, we explain the principle of damage imaging through the SLS technique and the problems in applying it to AM modeling and present a preliminary experiment with an aluminum alloy specimen conducted to examine the suitable conditions for the imaging. Finally, we describe the experiments performed on AM specimens with small defects.

2. Imaging of Subsurface Defects

The evaluation of the conditions of materials and components using ultrasonic waves generated and detected with laser is called laser ultrasonics, which has been widely used as a non-contact ultrasonic inspection [20, 21]. Because in-situ monitoring of AM components must be performed in a chamber of vacuum, argon, and nitrogen atmospheres, such a non-contact approach can be a promising technique. However, owing to several challenges, laser ultrasonics has not been adopted for in-situ monitoring of AM equipment. The first issue is the complex geometry as a result of AM, which makes the evaluation of internal defects using ultrasonic echoes difficult. In addition, in such an ultrasonic pulse echo technique, a high-frequency range (i.e., over 50 MHz) is used because the wavelength of the ultrasonic wave must be smaller than that of the targeted defects, and such a high-frequency range is not easily handled in in-situ inspections where the surface conditions of the object change during the process.

The authors have examined a method that can image delamination near the surface and wall thinning of the back of a thin plate using a non-contact measurement with no requirement for accurate adjustment [12–19]. In this method, called the SLS technique, a laser beam for generating ultrasonic waves is scanned with galvano mirrors, and ultrasonic waves are received at a fixed position. Because the reception point is not scanned, any ultrasonic reception device can be used, and very stable measurements would be possible when, for example, piezoelectric elements and ultrasonic transducers are attached to the object. Figure 1 shows a schematic diagram of the principle of imaging wall thinning of a thin plate using the SLS technique. When a laser beam for generating ultrasonic waves is irradiated on an intact thick area of a thin plate, the vibration energy is reduced, and the waveform at a fixed reception position appears small. By contrast, when the laser is irradiated on a damaged thin area of a plate, ultrasonic vibration is largely generated. In other words, when the laser beam for ultrasonic excitation is scanned with a galvano mirror and the vibration energy distribution is created from the signals for all excitation points, only the damage position provides an image with a large vibration. The authors have theoretically and experimentally verified this principle, which includes analyses of the resolution in the imaging technique [13], and the application to curved plate-like structures as pipes [14].

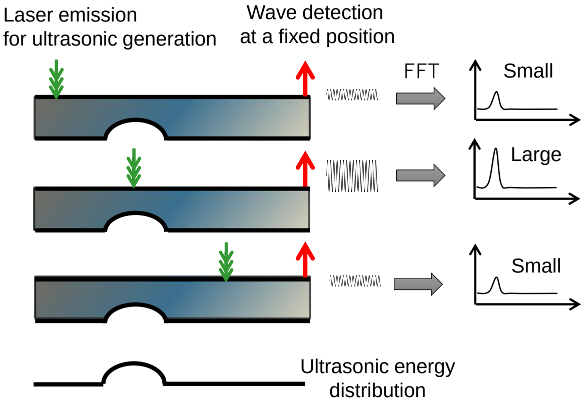

Fig. 1 Principle of imaging defects in a plate-like structure

Considering the characteristic of the imaging that uses the difference in the vibration energy generated at the laser irradiation point [17, 18], the authors demonstrated that defect images can be obtained even in complex structures using an acoustic field diffused within the whole structure. Because a diffuse acoustic field is formed by multiple complicated reflections in the object, this imaging technique would be suitable for a complex structure rather than a simple object.

For bulk materials, Solodov et al. [22, 23] and Rahammer and Kreutzbruck [24] performed damage detection using local defect resonance (LDR); in this technique, the entire structure vibrates at the frequency of local resonance at a delamination or a circular crack located near the surface in the bulk body, and the temperature rise of the local defect due to this resonance is detected by an infrared camera. The defect size considered in these studies was approximately a few millimeters, and the vibration frequency used for detection was some dozen kHz to 100 kHz. The authors also performed imaging of subsurface delamination in an aluminum alloy block using the SLS technique, in which a circular delamination with a diameter of 10 mm was imaged using a frequency range of 14–100 kHz [18].

In this study, we investigated imaging technique of defects with a diameter below 1.0 mm for in-situ monitoring in the AM process, and conducted experiments on subsurface defects with a diameter of 0.5 to 4.2 mm, assuming subsurface defects appearing in the AM process. Since the size of targeted defects is much smaller than those in our previous study, it is expected that a frequency range higher than those in previous studies should be used.

3. Experimental System

In a previous study [18], the authors modulated a high-repeating laser pulse output from a fiber laser device (G4 50W HS-S, SPI Laser) to generate burst and chirp ultrasonic waves below 100 kHz and acquired images of a circular delamination with a diameter of 10 mm near the surface. However, the modulation frequency limits the range to below a few hundred kHz, and ultrasonic waves in the high-frequency range beyond the MHz order cannot be excited using the modulation technique. Therefore, in this study, to detect small defects in the μm order using a high-frequency range, ultrasonic waves in the MHz range were excited using the laser pulse itself at a high repetition rate rather than ultrasonic vibration excitation using the amplitude modulation of the laser.

Figure 2 shows the experimental configuration of the specimen, laser apparatus, and ultrasonic transducers used in this study. A signal generator (USB-6343, National Instruments) provides a signal to control the laser pulse and a signal to control the galvano mirror scanner. The fiber laser equipment outputs the laser pulse following the trigger signal, and the mirror angle is adjusted such that the laser light is located at the desired point by the galvano mirror control signal. In this study, the trigger signal for the laser output is at the regular interval T_0 at a repetition frequency of $f_0 = (1/T_0 =$) 10 kHz or 100 kHz. Figure 3 shows the light intensity and ultrasonic signal received at a photo detector and an ultrasonic transducer, respectively, when a laser pulse train is provided at a repetition frequency of $f_0 = 10$ kHz and duration of 2 ms. The ultrasonic signal was detected with a pin-type transducer (VP-1093, Valpey Fisher; 2.3 mm diameter and 1.2 MHz nominal frequency range) attached to the back surface of an aluminum alloy plate measuring 40 mm × 40 mm × 3 mm. The detected waveforms were amplified by 40 dB with a preamplifier and then recorded using an analog–digital converter (PXI-5124, National Instruments). Large ultrasonic pulses appeared at a laser repetition frequency of $f_0 = 10$ kHz. In addition to the pulse train, noise-like waveforms were observed between pulsed ultrasonic waveforms, which represent a reverberation that travels back and forth through the specimen and consist of multiple resonant frequencies of the object [18]. Figure 4 shows the Fourier transform of the waveform shown in Fig. 3. The frequency range depended on the frequency characteristics of the ultrasonic transducer, and a large component was obtained below 3 MHz. The enlarged view of the frequency spectrum in the inset clearly shows that the frequency spectrum peak was repeated at intervals of $f_0 = 10$ kHz. This result can be explained by the Fourier analysis of repeated waveforms as follows.

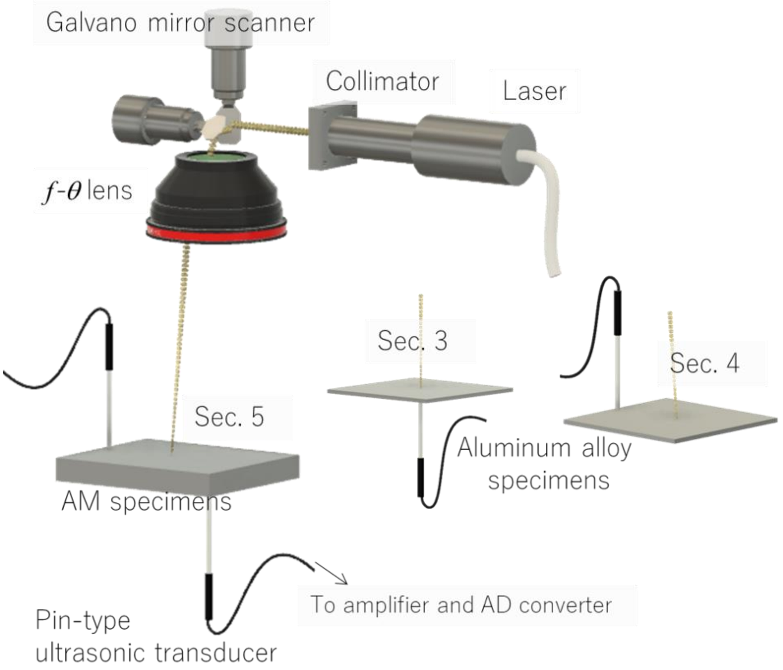

Fig. 2 Experimental configuration

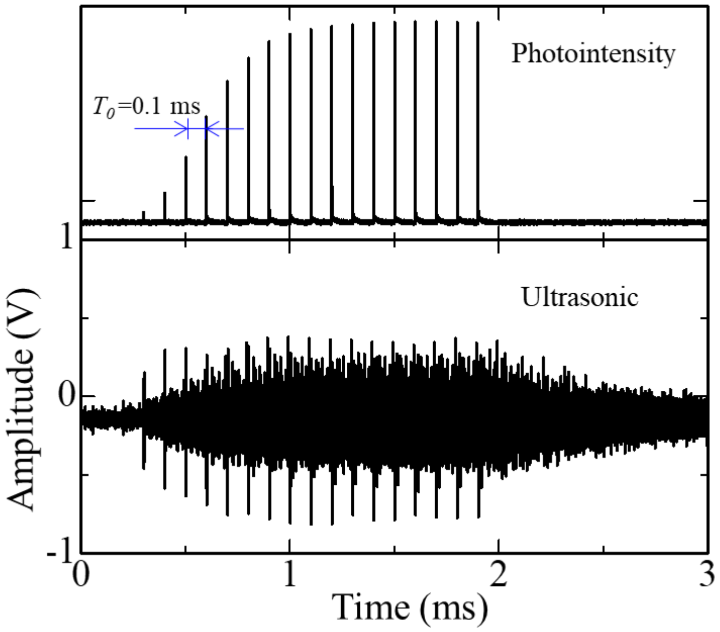

Fig. 3 Laser pulse train and generated ultrasonic waves

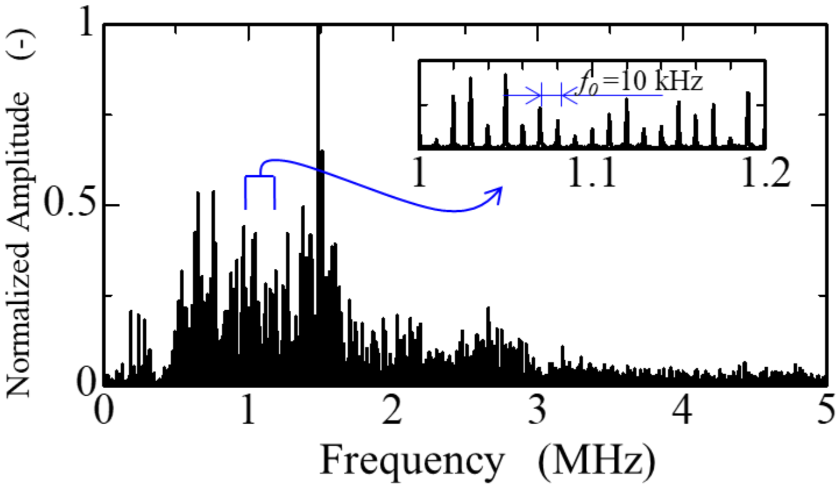

Fig. 4 Frequency spectrum of the ultrasonic wave in Fig. 3

With an ultrasonic single impulse wave $g(t)$, having a smaller pulse width than T_0, as shown in Fig. 5, the ultrasonic waveform generated by the repeated laser pulse irradiation $h(t)$ can be written as

$$h(t) = \sum_m g(t - mT_0)\,. \tag{1}$$

The Fourier transform of this waveform is

$$\begin{aligned} \mathcal{F}[h(t)] = H(\omega) &= \sum_m \mathcal{F}[g(t - mT_0)] = G(\omega) \sum_m e^{-i\omega m T_0}, \\ \Leftrightarrow H(f) &= G(f) \sum_m e^{-i2\pi m f/f_0}\,, \end{aligned} \tag{2}$$

where ω and f are the angular frequency and frequency and $G(\omega)$ and $H(\omega)$ are the Fourier transforms of the functions $g(t)$ and $h(t)$, respectively. When the summation of Eq. (2) ranges from $-\infty$ to $+\infty$, Eq. (2) is derived from the formulation of $\sum_m e^{-i2\pi m f/f_0} = f_0 \sum_m \delta(f - mf_0)$, as follows:

$$H(f) = f_0 G(f) \sum_{m=-\infty}^{+\infty} \delta(f - mf_0)\,. \tag{3}$$

That is, when the laser pulse irradiates at a repetition frequency of f_0, i.e., at the time interval of $T_0 (= 1/f_0)$, the Fourier spectrum of the waveform consists of discrete spectrum peaks at a regular interval of f_0. This principle is the same as that of the frequency comb used in the optical field, and the Fourier spectrum distribution corresponds to the spectral distribution of one pulse $|G(f)|$. In the experiments in this study, the spectral distribution was determined according to the characteristics of the ultrasonic transducer and the pulse width of the laser, and as a result, it ranged to a high-frequency range of the MHz order, as shown in Fig. 4. When considering a finite number of laser pulses, the peak value at $f = nf_0$ results in $H(nf_0) = NG(nf_0)$ from Eq. (2) and is proportional to the number of pulses N. That is, when considering actual measurements, the signal level increases as the number of pulses N increases, which leads to an easy analysis of the waveform.

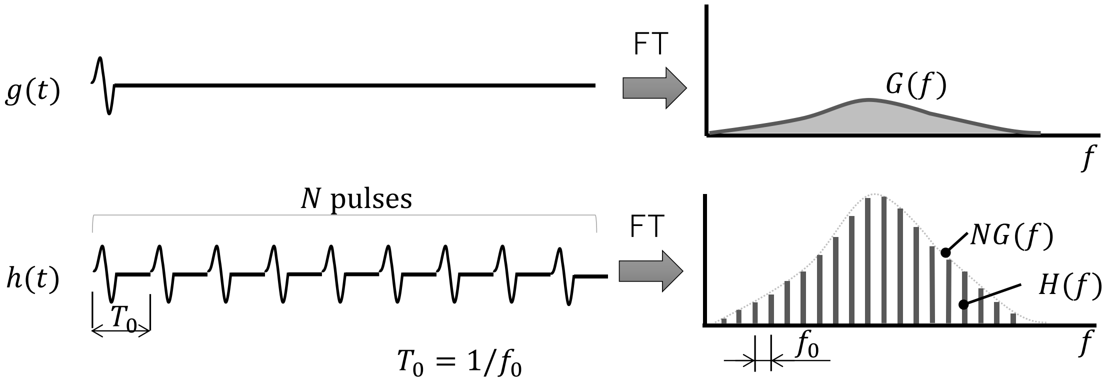

Fig. 5 Fourier transforms of the pulse wave and periodic pulse train

4. Preliminary Experiments with an Aluminum Alloy Specimen

First, as a specimen that can easily control the diameter and depth of defects, an aluminum alloy specimen fabricated by attaching a 0.3-mm-thick sheet to a 3.0-mm-thick plate with through holes (Fig. 6) was used. After drilling holes with diameters of 2.0, 2.5, 3.0, and 3.0 mm, the diameter, including the chamfer of the corner, was measured to be 2.8, 3.2, 3.6, and 4.2 mm, and the circles with these diameters were assumed to be artificially defective areas. The 0.3-mm-thick sheet and the 3.0-mm-thick plate were glued with two-part epoxy adhesives.

Figure 7 shows the images of artificial defects of these different diameters using the SLS technique, in which a repetition frequency f_0 of 10 kHz, duration of 8 ms, and laser output of approximately 50 W (average pulse energy = 5 mJ) were used, and the square sum of the digital signals at 20 ms after the moment of the laser irradiation recorded at a sample rate of 10 MHz was plotted as a shaded area. The square sum of radio frequency (RF) waveforms represents the energy of the waveform. If the waveform can be assumed as a diffusion field, then the wave energy is proportional to the vibration energy generated by the laser [17]. In addition, because the square sum of the RF signals is equal to the square sum of the frequency spectrum after the Fourier transform, the same result can be obtained even if the square sum of the discrete data after fast Fourier transform is taken. The waveforms were measured while moving at the 6.0 mm × 6.0 mm area on the artificial defect in 0.2 mm steps, and the energy distribution map was acquired. Because the maximum value in each figure is black, large vibration was measured when the laser was irradiated on the black part at the center, which indicates the existence of a hole near the surface. The black regions in all figures agree well with the size of the actual holes, which shows that imaging using the high-repetition pulse train can be performed appropriately. The black area in Fig. 7 (c) indicates that the image of a defect with a diameter of 3.6 mm was not circular and that the vibration was large in the upper left, which is considered to be a void due to the poor adhesion of the aluminum sheets.

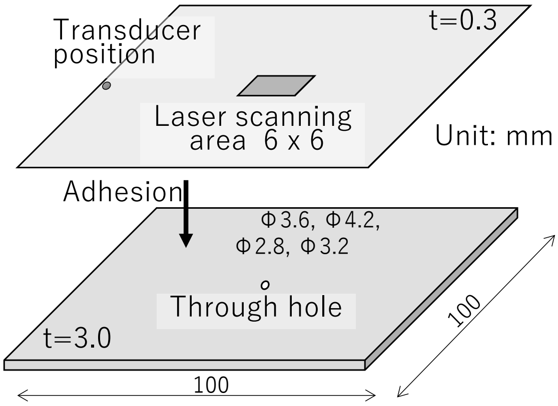

Fig. 6 Aluminum alloy plate specimen for fundamental experiments

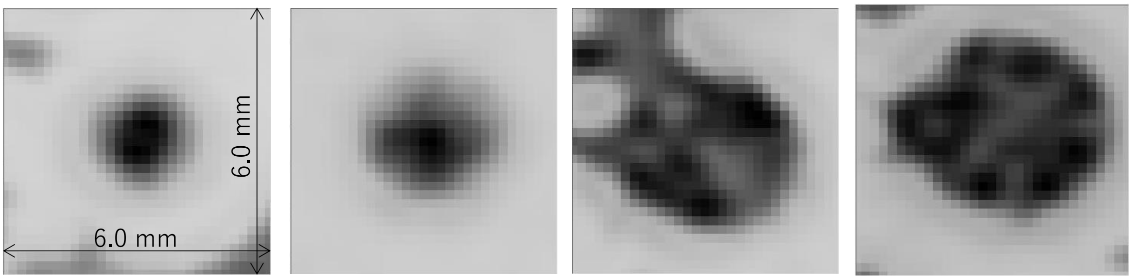

(a) 2.8 mm (b) 3.2 mm (c) 3.6 mm (d) 4.2 mm

Fig. 7 Images of subsurface holes with various diameters

As described in Section 3, the signal level is improved according to the number N of pulses of the laser output. To investigate the effect of images on the number of pulses, Fig. 8 shows defect images for different laser output durations of 1, 2, and 8 ms. All images were obtained for artificial defects with a diameter of 3.2 mm, and the parameters other than the laser output duration were the same as those in Fig. 7. In the case of 1 ms (Fig. 8 (a)), the difference in intensity between the black area and surrounding gray area is small. This result is attributed to the relatively large noise level because the square sum of the recorded waveform is small for the duration of 1 ms. Meanwhile, in the case of 8 ms, the signal can be obtained under a suitable signal-to-noise ratio (SNR) with a large difference between the black region and the surrounding area.

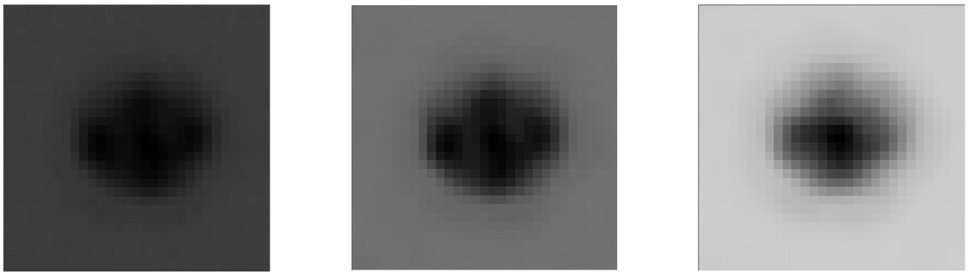
(a) 1 ms (b) 2 ms (c) 8 ms

Fig. 8 Comparison of defect images in different time durations of laser emission
The diameter of a subsurface hole is 3.2 mm.

Next, to examine the frequency range suitable for defect detection, a similar image was created using the square sum of the frequency spectrum data between different frequency gates. Figure 9 shows the imaging results with different frequency gates for the artificial defect with a diameter of 3.2 mm. The same waveform data were used as in Fig. 7 (b). Figures 9 (a)–(e) show the results when changing the upper limit of the gate by 20 kHz; a significant image change between (c) and (d) can be observed. That is, (a)–(c) have a small signal level and relatively large noise; thus, the dark-gray area spreads over the entire region. However, in (d), a circle indicating an artificial defect appears clearly, and the image hardly changes even if the frequency upper limit is raised to 400 kHz, as shown in (f). This result shows that a very large vibration appeared in the defective part at approximately 250 kHz.

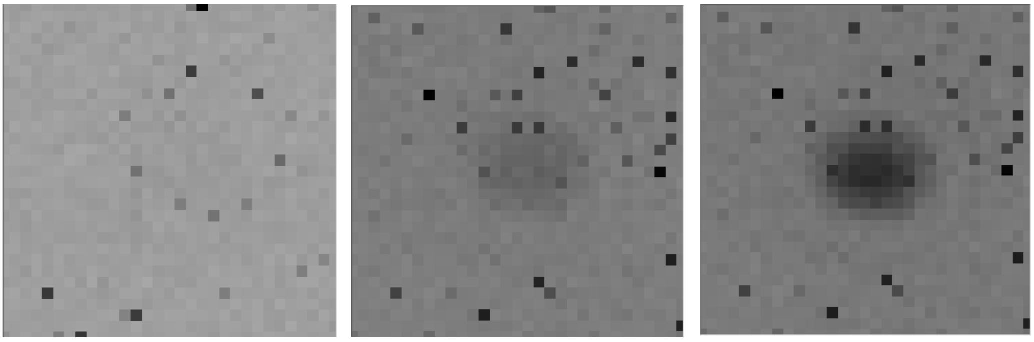
(a) 0–200 kHz (b) 0–220 kHz (c) 0–240 kHz

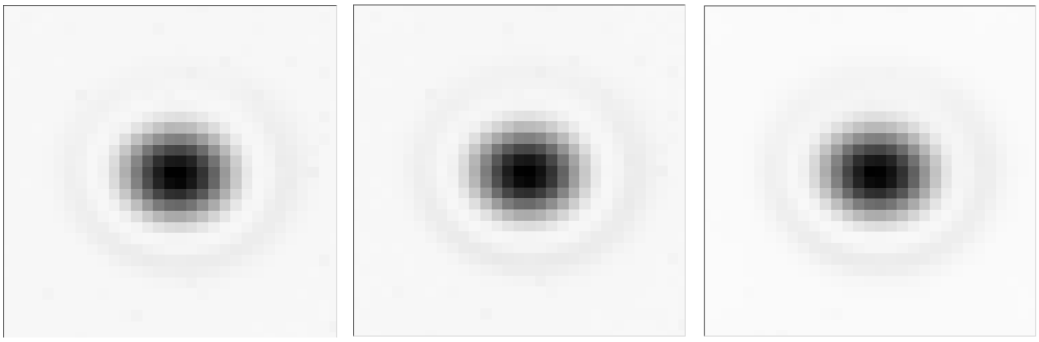

(d) 0–260 kHz (e) 0–280 kHz (f) 0–400 kHz

Fig. 9 Comparison of defect images in various frequency ranges
The diameter of a subsurface hole is 3.2 mm.

The following approximated solution provides a theoretical analysis for this phenomenon [22, 24].

$$f_{LDR} \approx \frac{1.6h}{(d/2)^2}\sqrt{\frac{E}{12\rho(1-\nu^2)}} \tag{4}$$

This is the approximated solution of the local resonant frequency of the fundamental mode at the circular flat bottom hole with a diameter of d located at a depth of h from the surface, which is effective when the flat bottom area vibrates as a circular thin disk with fixed surroundings. $E, \nu,$ and ρ represent the Young's modulus, Poisson's ratio, and density of a material, respectively. Figure 10 shows the relationship between the local resonant frequency f_{LDR} and the diameter of the hole d for aluminum alloys with $= 70$ GPa, $\nu = 0.33$, and $\rho = 2.7 \times 10^3$ kg/m^3. For $d = 3.2$ mm in Eq. (4), $f_{LDR} = 292$ kHz, which is equivalent to the frequency that was experimentally obtained (Fig. 9) as a large resonant frequency at a defect of the same size. Similarly, the resonant frequencies were experimentally measured for holes with other sizes, such as 310 and 130 kHz for diameters of 2.8 and 4.2 mm, respectively. For a diameter of 3.6 mm, a threshold frequency that considerably changes the image cannot be clearly seen, because of the very large vibration in the areas of poor adhesion. The aforementioned experimental results, plotted in Fig. 10 with circles, agree with the theoretical approximated curve expressed in Eq. (4). Thus, the large vibration is the resonance at a thin circular disk on a hole, and we can predict the resonant frequency using Eq. (4).

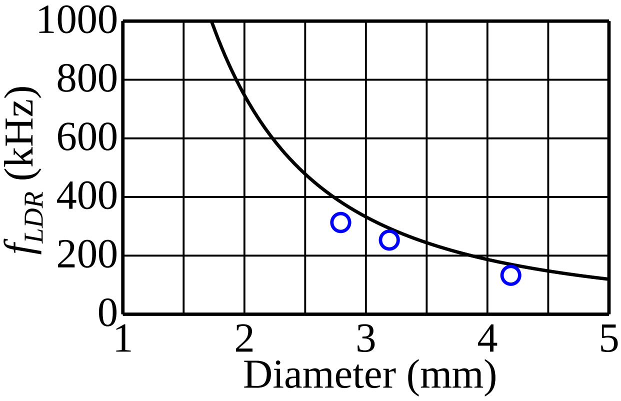

Fig. 10 Local defect resonance frequency

Next, to investigate the effect of repetition frequencies on the image, the defect images were obtained with a repetition frequency of $f_0 = 100$ kHz (Fig. 11); the other parameters were the same as those in Fig. 7. Although a defect area can be identified in all the figures, spotted patterns were observed in the defect area. This is the effect of the higher resonance modes in the circular defect area. For a repetition frequency of 100 kHz, discrete peaks of the frequency spectrum, as shown in Figs. 4 and 5, appear every 100 kHz. Moreover, the LDRs of the first mode of the circular defect were approximately 310, 250, and 130 kHz for (a), (b), and (d), respectively, as shown in Fig. 9. Therefore, if there is no LDR at a frequency of an exact multiple of 100 kHz, then the first mode vibrating the entire circular area with the same phase becomes more unlikely to appear. Figures 11 (a)–(d) seem to have a spotted pattern because of the large influence of a higher mode with a resonant point at a multiple of 100 kHz than the frequency LDR in the primary mode.

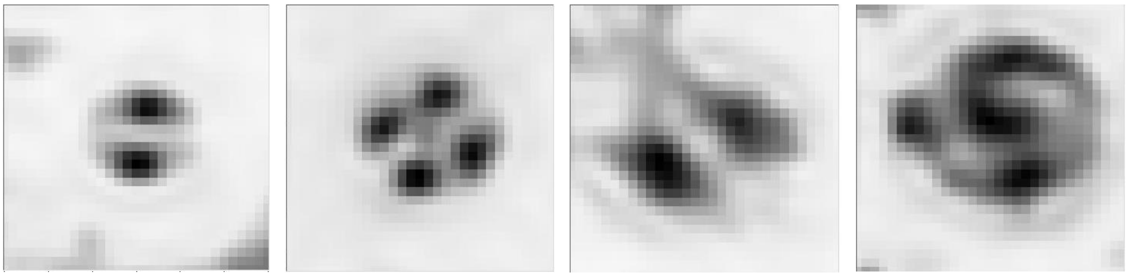

(a) 2.8 mm (b) 3.2 mm (c) 3.6 mm (d) 4.2 mm

Fig. 11 Images of subsurface holes with various diameters at a repetition frequency of 100 kHz

5. Application Experiments of AM Components

The imaging technique was applied to Inconel's AM body with small artificial defects. AM specimens with dimensions of 100 × 100 × 10 mm^3 were fabricated using selective laser melting, in which the laser beam was intentionally irradiated insufficiently at cylindrical regions located below 0.25 mm from the top surface to create defect regions. The defect regions were supposed to be a cylindrical shape with diameters of 0.5, 0.8, and 1.5 mm and a length of 1.0 mm, and an unfused Inconel powder remained inside. Considering in-situ inspection in the next step, the surface of the specimens was not polished. Laser scanning areas of 4.0 × 4.0 mm^2 were directly located above the artificial defect in 0.1 mm steps, with a repetition frequency of $f_0 =$ 10 kHz. The shaded image was obtained by plotting the sum of the square of the recorded signal. Figure 13 shows the defect images when an ultrasonic transducer is in contact with the same surface as the laser irradiation surface. In all cases, a black area indicating the defect appeared near the center, but for the smallest defect with a diameter of 0.5 mm, the difference from the surroundings was small, and the defect image became less clear.

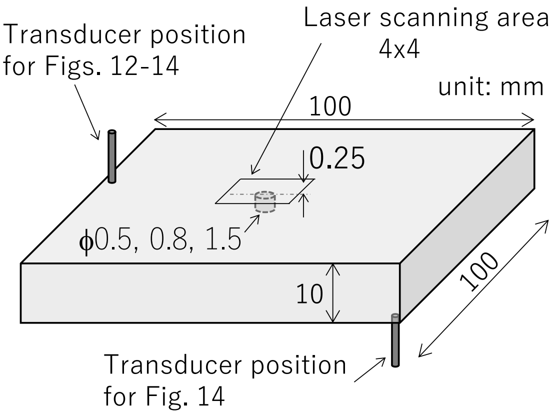

Fig. 12 AM specimen and transducer positions

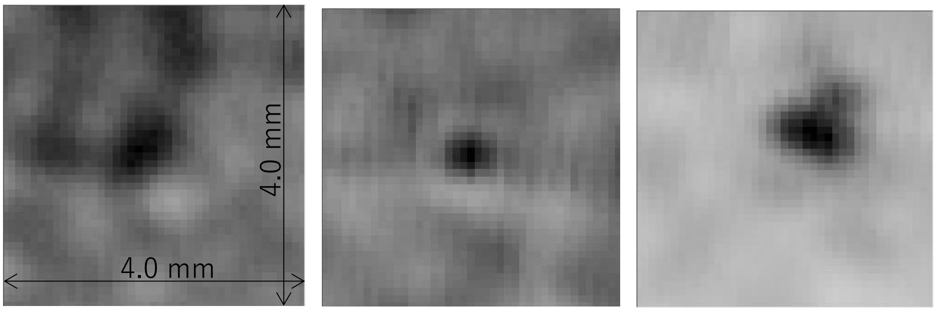

(a) ϕ 0.5 mm (b) ϕ 0.8 mm (c) ϕ 1.5 mm

Fig. 13 Images of AM specimens with different defect diameters

The tendency observed in the image of the defect in the AM specimens can also be explained by the local resonance at the defect area. Figure 14 shows the defect images for a diameter of 0.8 mm shown in Fig. 13 (b), obtained by setting different frequency gates. The defect image could not be obtained at 1.0 MHz or less (Fig. 14(a)), but the defect image gradually became clearer when the gate expanded to the high-frequency side. This result implies that the LDR is approximately 1.2–1.6 MHz.

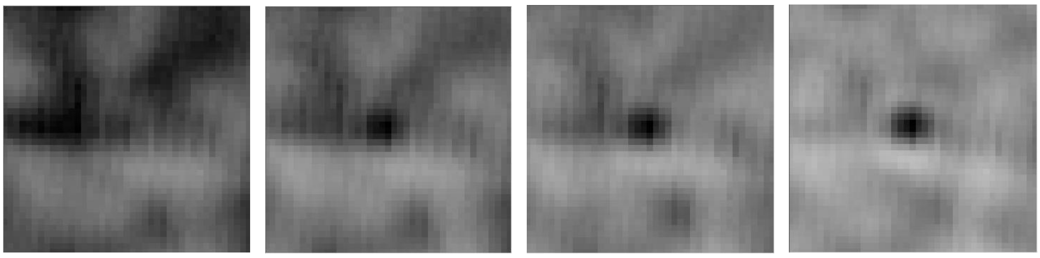

(a) 0.0–1.0 MHz (b) 0.0–1.2 MHz (c) 0.0–1.4 MHz (d) 0.0–1.6 MHz

Fig. 14 Images of the defect with 0.8 mm diameter with different frequency gates

The solid line in Fig. 15 presents the theoretical solution to Eq. (4) for this AM specimen, where the material constants of Inconel were assumed to be $E = 77.2$ GPa, $\nu = 0.32$, and $\rho = 8.19 \times 10^3$ kg/m^3, and the distance between the surface and the artificial defect was $h = 0.25$ mm. In addition, the LDRs obtained with finite element analysis (FEA) using COMSOL Multiphysics ® are shown as a dashed line in Fig. 15. The LDRs were calculated with the eigen mode analysis for the rectangular parallelepiped specimen with a dimension of $5.0 \times 5.0 \times 2.0$ mm^3, having a cylindrical cavity with diameters of 1.6, 2.0, 2.5, and 3.0 mm and a length of 1.0 mm at 0.25 mm depth from the surface. Among the many resonant modes obtained in the finite element calculation, the resonant modes with large vibrations at the defect were selected. Because the purpose of the calculation is to find the locally resonant modes at the defect, the size of the specimen was set smaller than that of the actual specimen to reduce the calculation time and memory.

At a diameter of 2.0 mm or more, the approximate theoretical solution and FEA solution were almost the same, but in the small diameter range (<2.0 mm), the FEA solution showed a smaller resonant frequency. This finding means that the theoretical solution in Eq. (4) is effective only when the thickness of a circular disk h is sufficiently small compared with the diameter d, and the LDR calculated with the FEA must be used for the defect in the small-diameter range. The LDR for a defect with a diameter of

0.8 mm based on the FEA was 1.46 MHz, which agrees well with the experimental result, as shown in Fig. 14.

Furthermore, the LDR at a diameter of 0.5 mm from FEA was approximately 2.0 MHz. As shown in Fig. 4, this frequency is outside the frequency range of the ultrasonic transducer, and as a result of the small signal level, the image becomes unclear in Fig. 13 (a).

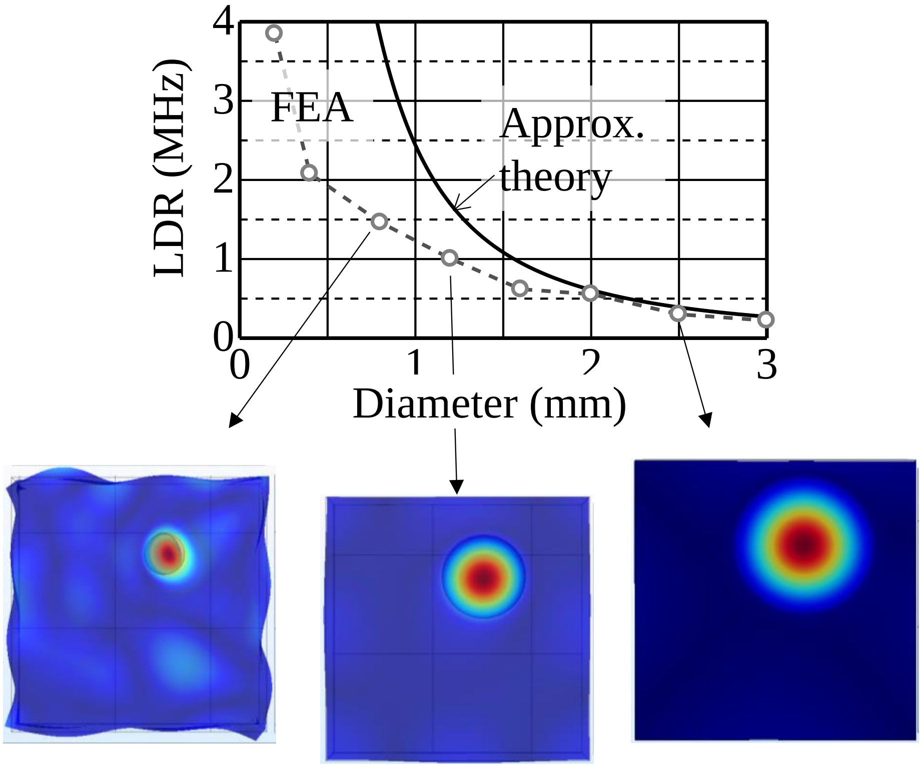

Fig. 15 LDR calculated by Eq. (4) and FEA

Considering the in-situ inspection in the AM process, the ultrasonic transducer cannot be on the surface of the AM object. Thus, in the future, it must be placed on a build plate that supports the back surface of the AM object. To study this possibility, we also examined the inspection where ultrasonic waves were measured by the transducer on the back side of the AM object, as shown in Fig. 12. Figure 16 shows the defect images when received simultaneously on the front and back sides for the same laser irradiation. The defect images were properly acquired but were unclear in (b) because the signal level was slightly lower on the back side.

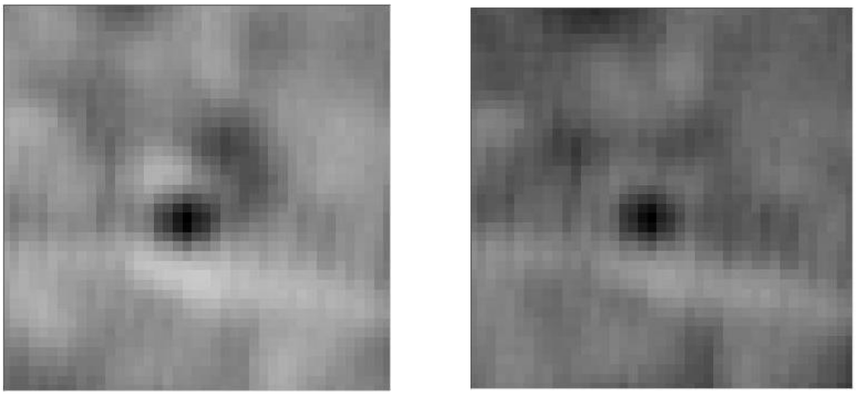

(a) Top surface (b) Back surface

Fig. 16 Images of the 0.8-mm-diameter defect using waveforms detected on the top and back surfaces

This imaging technique using a diffusion field has a prominent feature in that the image can be obtained without depending on the transducer position. Therefore, once a transducer is placed on the build plate, a similar imaging inspection can be conducted. In addition, as shown in Fig. 16, because multiple defect images can be acquired simultaneously using multiple transducers, synthesizing these images improves the defect detection ability [19]. Furthermore, by analyzing the LDR, the required frequency range was determined for the defects to be found. Thus, in the future, a suitable experimental system, such as ultrasonic transducers and amplifiers, should be designed.

Because AM objects are shaped by stacking thin layers, the entire body can be inspected by incorporating the inspection process of this method, which can detect defects in thin layers in the AM process. Furthermore, imaging inspection can be feasible only by adding an ultrasonic detector that receives ultrasonic waves to the AM system of SLM because it can share a laser scanning mechanism and laser device.

6. Conclusions

This paper discusses an imaging technique for minute defects that appear in AM components using ultrasonic waves generated by laser irradiation. First, to use ultrasonic waves in the MHz range, we described a method of using high-repetition pulses and showed that the frequency range depends on the pulse width of the laser and the frequency characteristic of the receiving device and that the SNR shows greater improvement with the number of pulses. Furthermore, defect imaging experiments using artificial defect specimens of aluminum alloy plates revealed that defect images are highly dependent on local resonant frequencies at a defect and that clearer images can be obtained using the frequency range that includes the LDR. Furthermore, experiments using AM specimens with defect diameters of 0.5, 0.8, and 1.5 mm proved that the imaging technique can create an image of a defect that could not detect in our previous studies using the SLS. The experimental results provided the guideline that the LDR frequencies of targeted defects must be included in the tested frequency range.

Acknowledgments

This work was supported by Japan Society for the Promotion of Science KAKENHI [grant number 18K18920].

References

[1] A. Thompson, I. Maskery, R.K. Leach, X-ray computed tomography for additive manufacturing: A review, Meas. Sci. Technol. 27 (2016). https://doi.org/10.1088/0957-0233/27/7/072001.

[2] M. Grasso, B.M. Colosimo, Process defects and in situ monitoring methods in metal powder bed fusion: A review, Meas. Sci. Technol. 28 (2017). https://doi.org/10.1088/1361-6501/aa5c4f.

[3] M. Hirsch, R. Patel, W. Li, G. Guan, R.K. Leach, S.D. Sharples, A.T. Clare, Assessing the capability of in-situ nondestructive analysis during layer based additive manufacture, Addit. Manuf. 13 (2017) 135–142. https://doi.org/10.1016/j.addma.2016.10.004.

[4] T. Sol, S. Hayun, D. Noiman, E. Tiferet, O. Yeheskel, O. Tevet, Nondestructive ultrasonic evaluation of additively manufactured AlSi10Mg samples, Addit. Manuf. 22 (2018) 700–707. https://doi.org/10.1016/j.addma.2018.06.016 .

[5] C. Gobert, E.W. Reutzel, J. Petrich, A.R. Nassar, S. Phoha, Application of supervised machine learning for defect detection during metallic powder bed fusion additive manufacturing using high resolution imaging., Addit. Manuf. 21 (2018) 517–528. https://doi.org/10.1016/j.addma.2018.04.005.

[6] R. Patel, M. Hirsch, P. Dryburgh, D. Pieris, S. Achamfuo-Yeboah, R. Smith, R. Light, S. Sharples, A. Clare, M. Clark, Imaging material texture of as-deposited selective laser melted parts using spatially resolved acoustic spectroscopy, Appl. Sci. 8 (2018). https://doi.org/10.3390/app8101991 .

[7] D. Cerniglia, N. Montinaro, Defect Detection in Additively Manufactured Components: Laser Ultrasound and Laser Thermography Comparison, Procedia Struct. Integr. 8 (2018) 154–162. https://doi.org/10.1016/j.prostr.2017.12.016.

[8] N. Montinaro, D. Cerniglia, G. Pitarresi, Defect detection in additively manufactured titanium prosthesis by flying laser scanning thermography, Procedia Struct. Integr. 12 (2018) 165–172. https://doi.org/10.1016/j.prostr.2018.11.098.

[9] C. Mandache, Overview of non-destructive evaluation techniques for metal-based additive manufacturing, Mater. Sci. Technol. (United Kingdom). 35 (2019) 1007–1015. https://doi.org/10.1080/02670836.2019.1596370.

[10] F. Honarvar, A. Varvani-Farahani, A review of ultrasonic testing applications in additive manufacturing: Defect evaluation, material characterization, and process control, Ultrasonics. 108 (2020) 106227. https://doi.org/10.1016/j.ultras.2020.106227 .

[11] F. Simonetti, I.L. Satow, A.J. Brath, K.C. Wells, J. Porter, B. Hayes, K. Davis, Cryo-Ultrasonic NDE: Ice-Cold Ultrasonic Waves for the Detection of Damage in Complex-Shaped Engineering Components, IEEE Trans. Ultrason. Ferroelectr. Freq. Control. 65 (2018) 638–647. https://doi.org/10.1109/TUFFC.2018.2796387.

[12] T. Hayashi, Imaging defects in a plate with complex geometries, Appl. Phys. Lett. 108 (2016) 081901. https://doi.org/10.1063/1.4942599.

[13] T. Hayashi, M. Fukuyama, Vibration energy analysis of a plate for defect imaging with a scanning laser source technique, J. Acoust. Soc. Am. 140 (2016) 2427–2436. https://doi.org/10.1121/1.4964275.

[14] T. Hayashi, Non-contact imaging of pipe thinning using elastic guided waves generated and detected by lasers, Int. J. Press. Vessel. Pip. 153 (2017) 26–31. https://doi.org/10.1016/j.ijpvp.2017.05.006.

[15] T. Hayashi, K. Ishihara, Generation of narrowband elastic waves with a fiber laser and its application to the imaging of defects in a plate, Ultrasonics. 77 (2017) 47–53. https://doi.org/10.1016/j.ultras.2017.01.016.

[16] T. Hayashi, High-speed non-contact defect imaging for a plate-like structure, NDT E Int. 85 (2017) 53–62. https://doi.org/10.1016/j.ndteint.2016.10.009.

[17] T. Hayashi, Defect imaging for plate-like structures using diffuse field, J. Acoust. Soc. Am. 143 (2018) EL260–EL265. https://doi.org/10.1121/1.5030915.

[18] S. Nakao, T. Hayashi, Non-contact imaging for delamination using diffuse field concept, Japan Soc. Appl. Phys. 58 (2019) SGGB07. https://doi.org/10.7567/1347-4065/ab0ada

[19] T. Hayashi, M. Murase, N. Ogura, T. Kitayama, Imaging Defects in a Plate with Full Non-Contact Scanning Laser Source Technique, Mater. Trans. 55 (2014) 1045–1050. https://doi.org/10.2320/matertrans.I-M2014817.

[20] C.B. Scruby and L.E. Drain, Laser Ultrasonics: Techniques and Applications (Adam Hilger, Bristol, Philadelphia, and NewYork, 1990).

[21] M. Clark, S.D. Sharples, M.G. Somekh, Fast, all-optical rayleigh wave microscope: imaging on isotropie and anisotropie materials, IEEE Trans. Ultrason. Ferroelectr. Freq. Control. 47 (2000) 65–74. https://doi.org/10.1109/58.818749.

[22] I. Solodov, J. Bai, G. Busse, Resonant ultrasound spectroscopy of defects: Case study of flat-bottomed holes, J. Appl. Phys. 113 (2013). https://doi.org/10.1063/1.4810926.

[23] I. Solodov, D. Derusova, M. Rahammer, Thermosonic Chladni figures for defect-selective imaging, Ultrasonics. 60 (2015) 1–5. https://doi.org/10.1016/j.ultras.2015.02.007.

[24] M. Rahammer, M. Kreutzbruck, Fourier-transform vibrothermography with frequency sweep excitation utilizing local defect resonances, NDT E Int. 86 (2017) 83–88. https://doi.org/10.1016/j.ndteint.2016.11.012.

Click here to access/download;Figure;Figures.docx

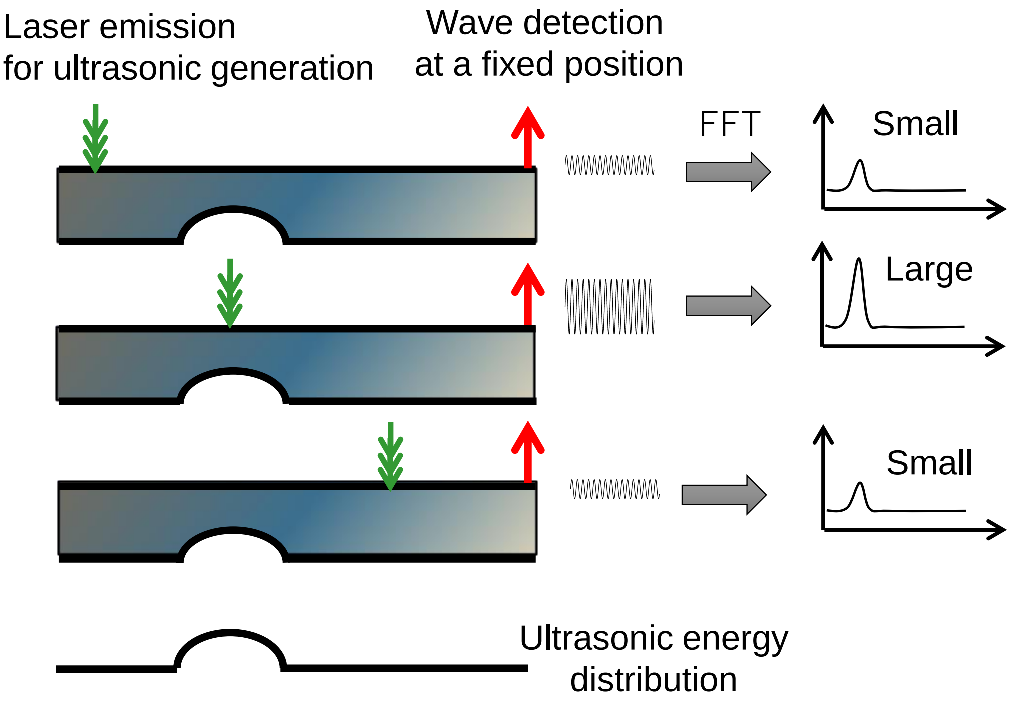

Fig. 1 Principle of imaging defects in a plate-like structure

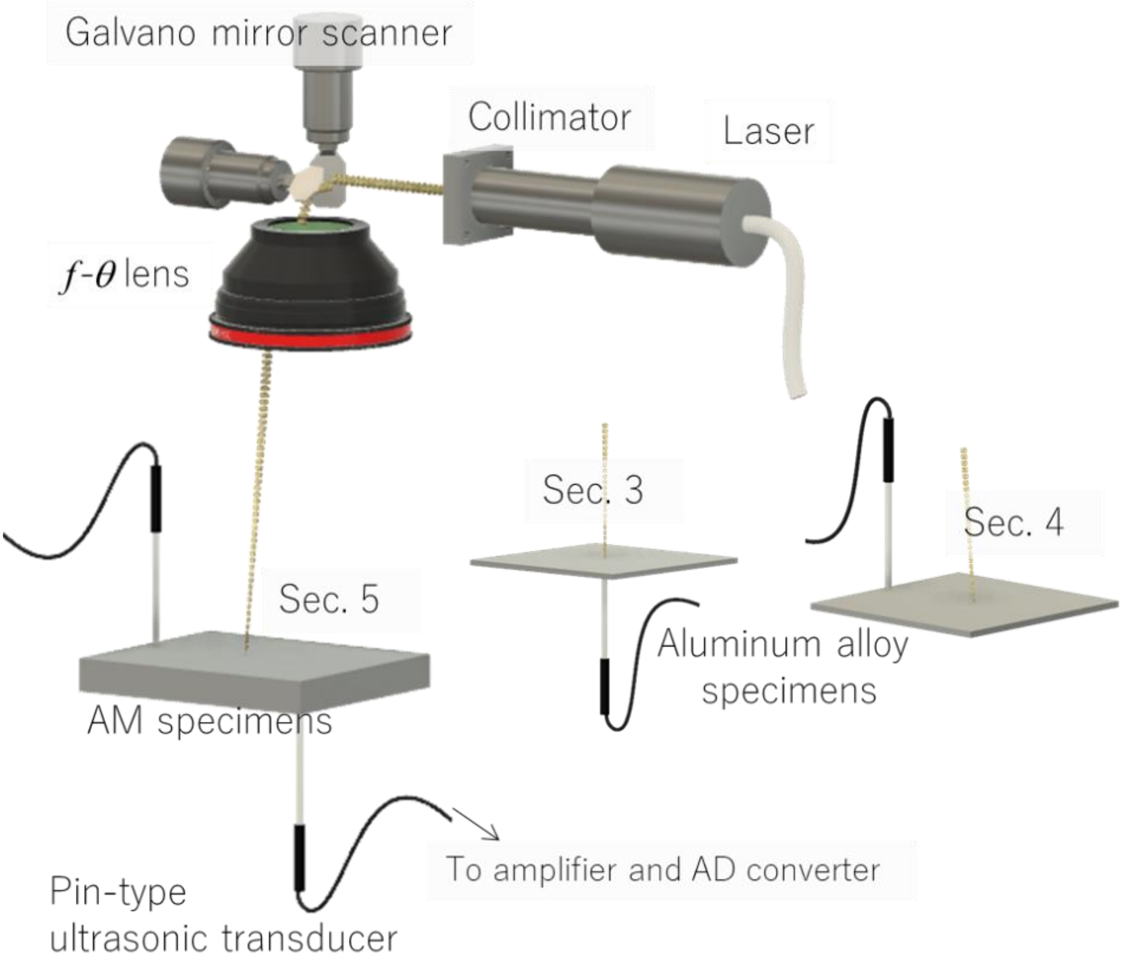

Fig. 2 Experimental configuration

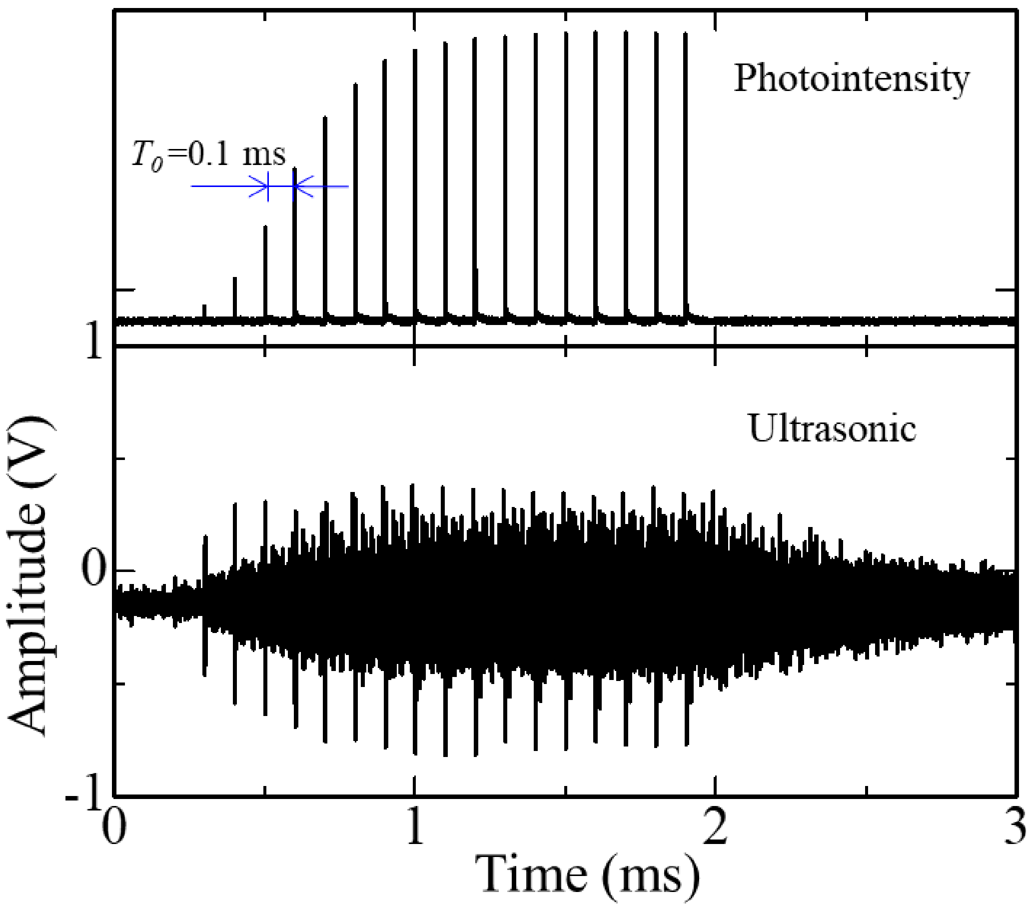

Fig. 3 Laser pulse train and generated ultrasonic waves

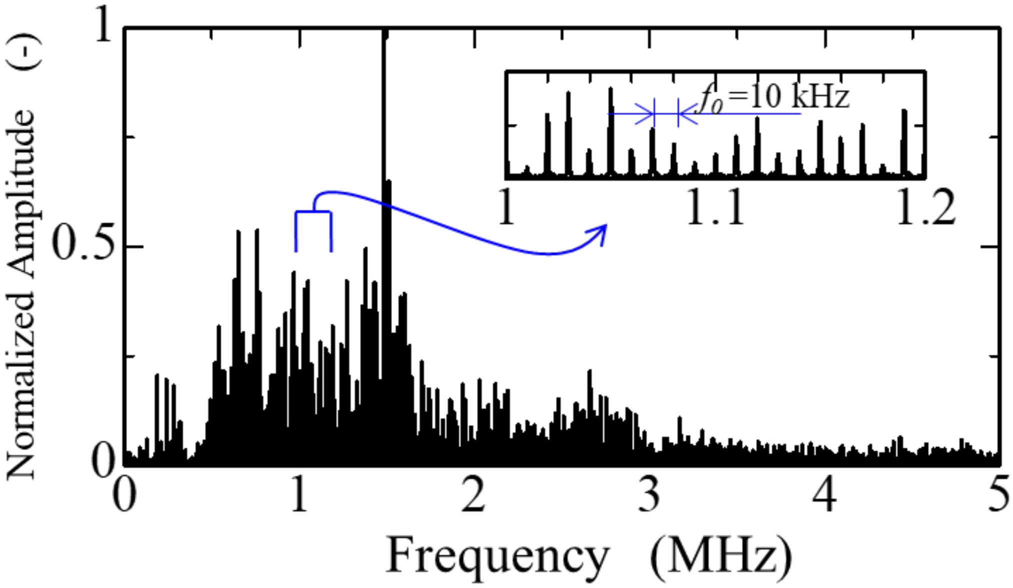

Fig. 4 Frequency spectrum of the ultrasonic wave in Fig. 3

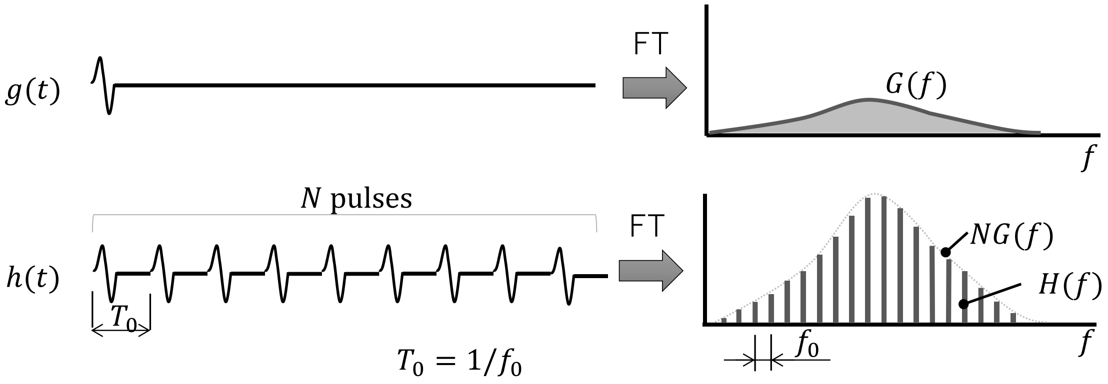

Fig. 5 Fourier transforms of the pulse wave and periodic pulse train

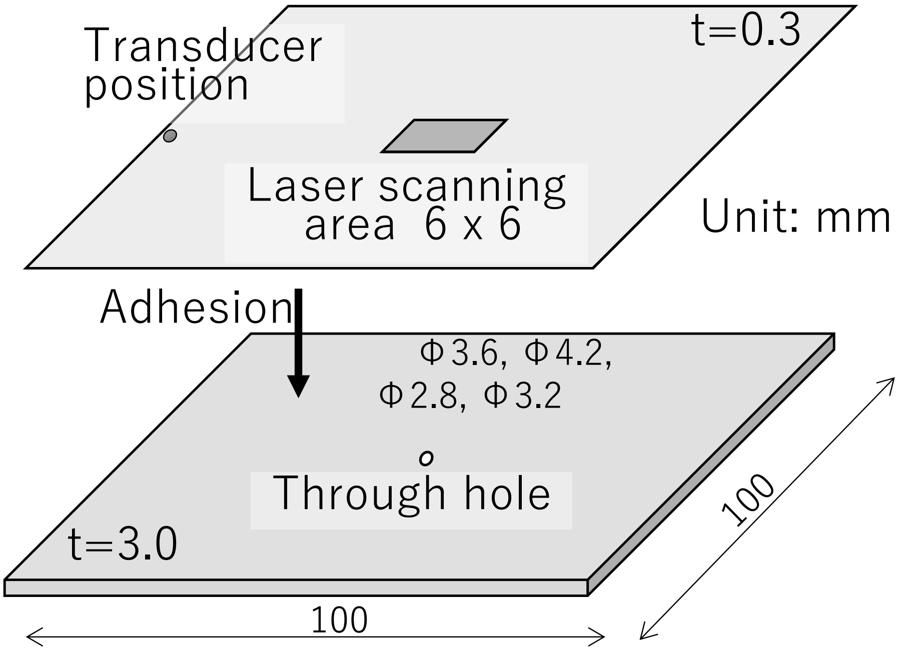

Fig. 6 Aluminum alloy plate specimen for fundamental experiments

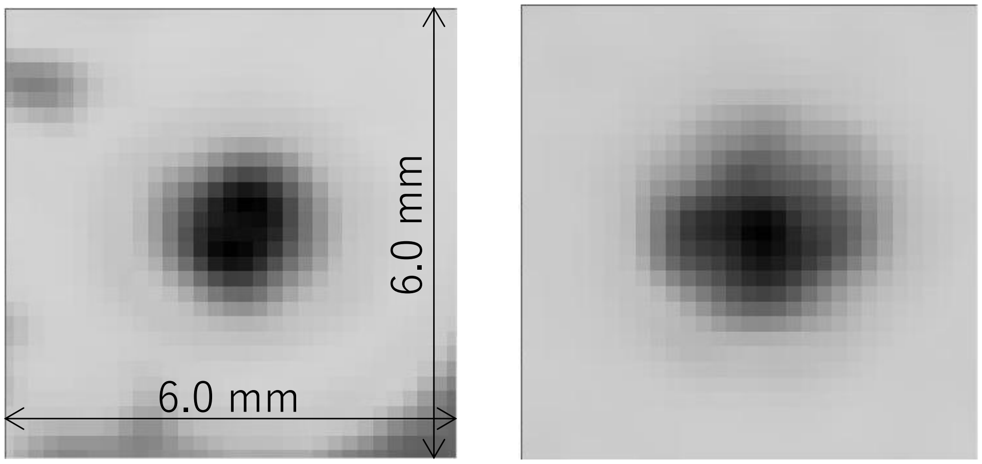

(a) 2.8 mm (b) 3.2 mm

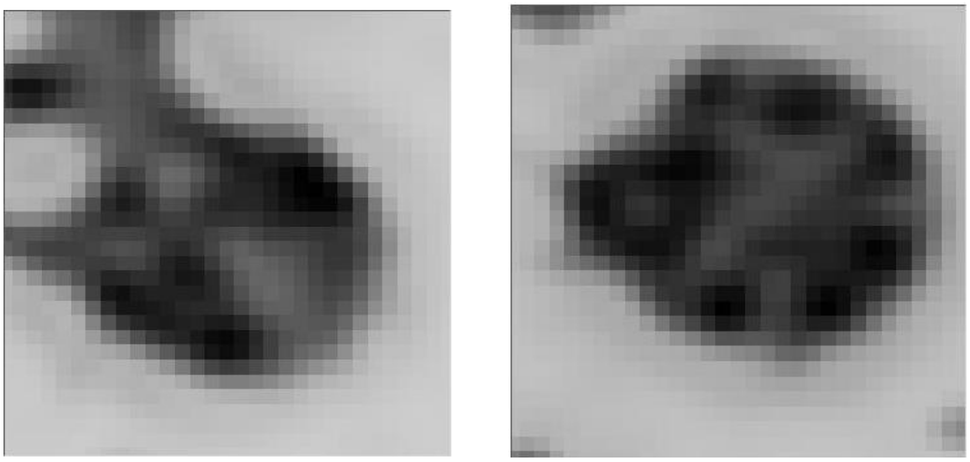

(c) 3.6 mm (d) 4.2 mm

Fig. 7 Images of subsurface holes with various diameters

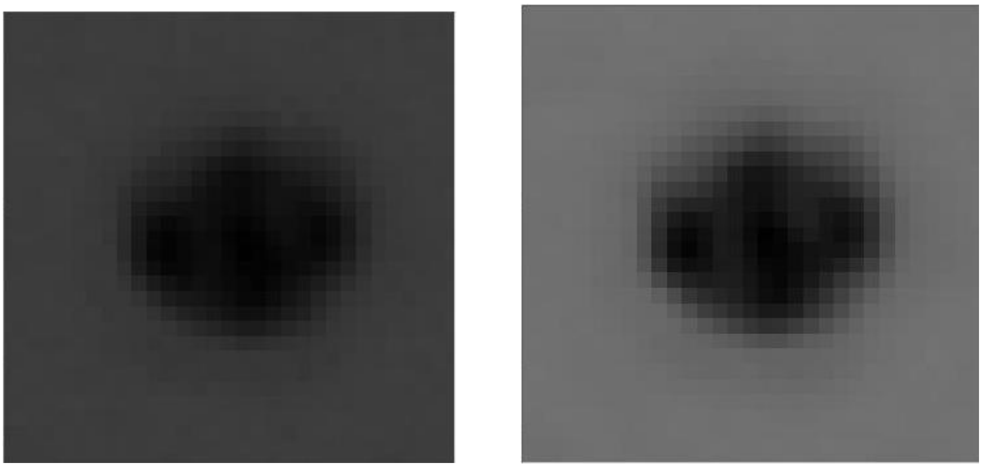

(a) 1 ms (b) 2 ms

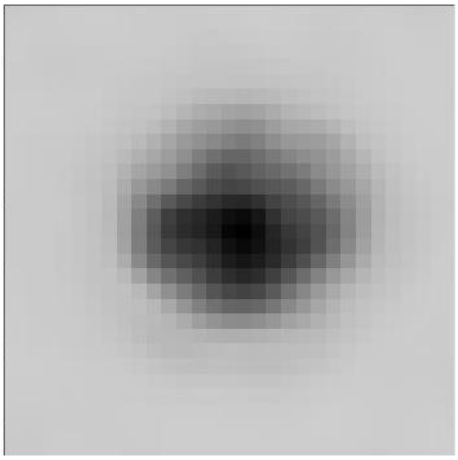

(c) 8 ms

Fig. 8 Comparison of defect images in different time durations of laser emission
The diameter of a subsurface hole is 3.2 mm.

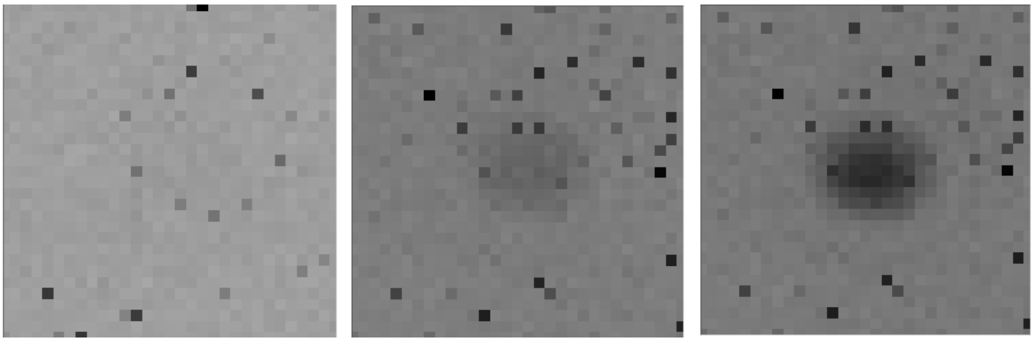

(a) 0–200 kHz (b) 0–220 kHz (c) 0–240 kHz

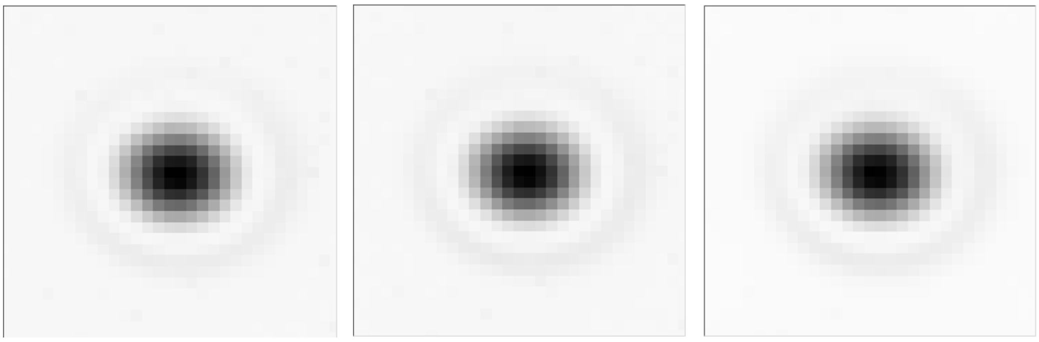

(d) 0–260 kHz (e) 0–280 kHz (f) 0–400 kHz

Fig. 9 Comparison of defect images in various frequency ranges
The diameter of a subsurface hole is 3.2 mm.

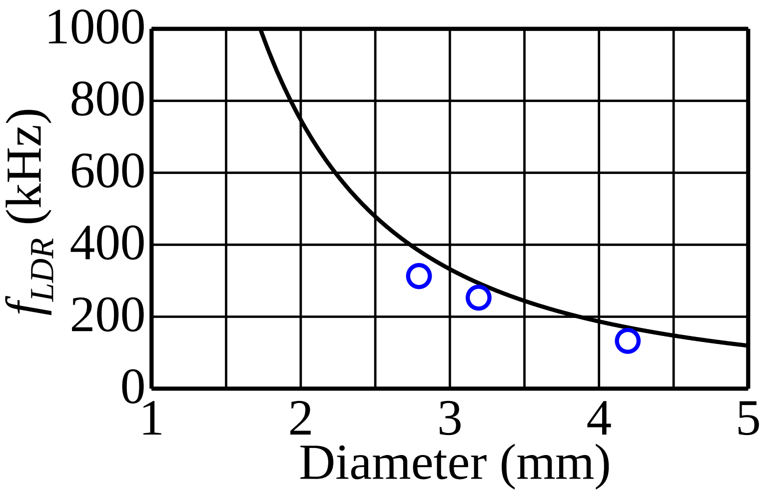

Fig. 10 Local defect resonance frequency

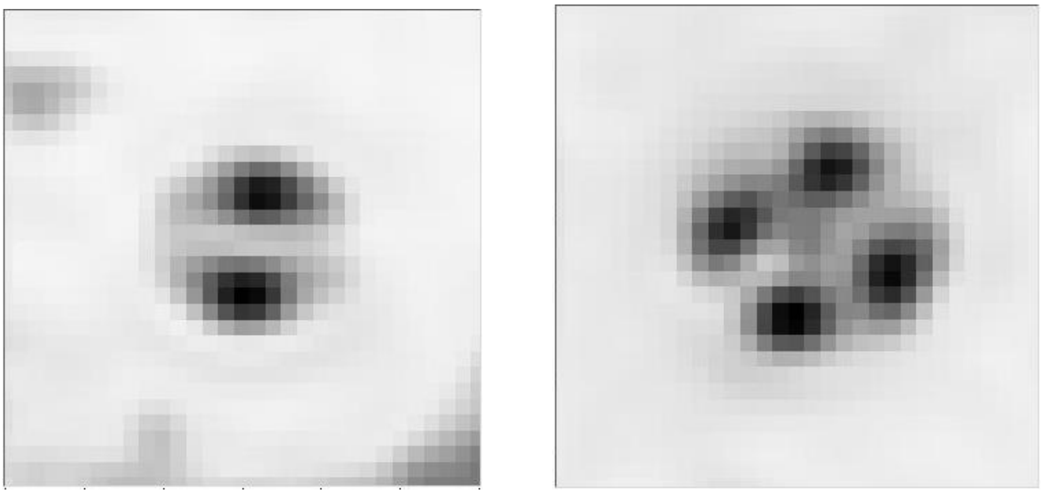

(a) 2.8 mm (b) 3.2 mm

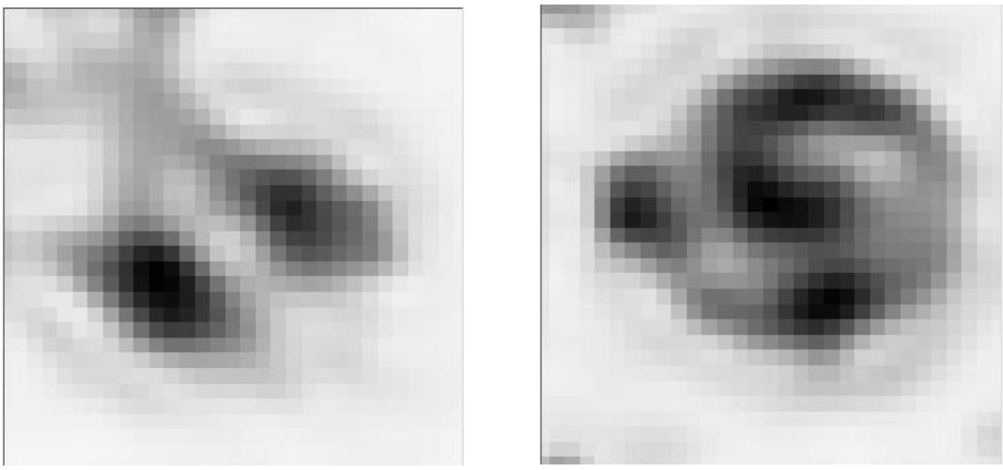

(c) 3.6 mm (d) 4.2 mm

Fig. 11 Images of subsurface holes with various diameters at a repetition frequency of 100 kHz

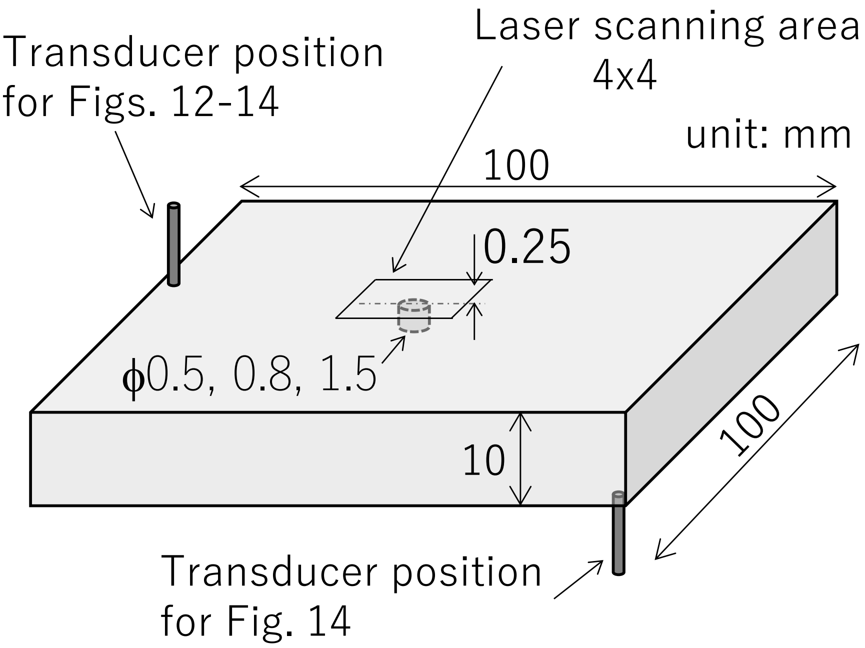

Fig. 12 AM specimen and transducer positions

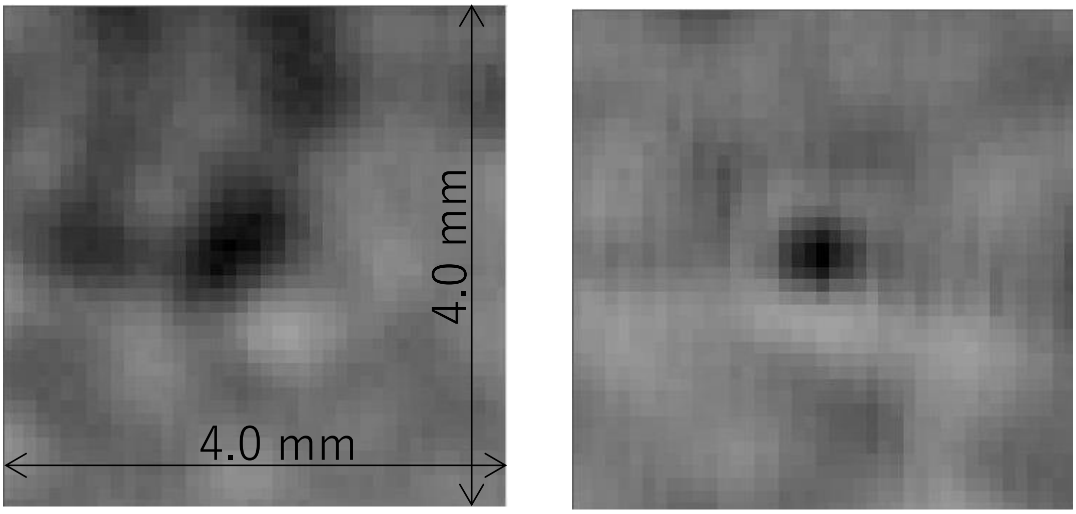

(a) ϕ 0.5 mm (b) ϕ 0.8 mm

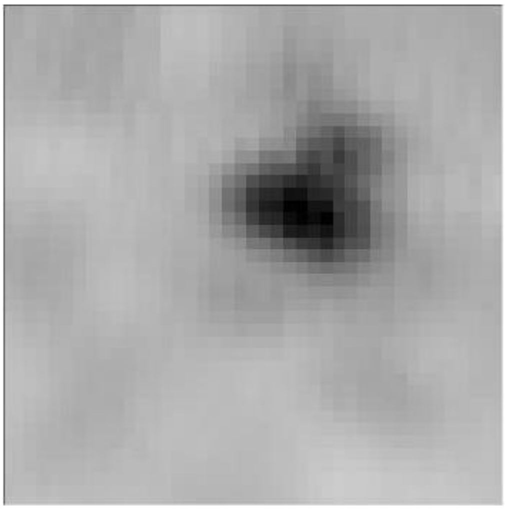

(c) ϕ 1.5 mm

Fig. 13 Images of AM specimens with different defect diameters

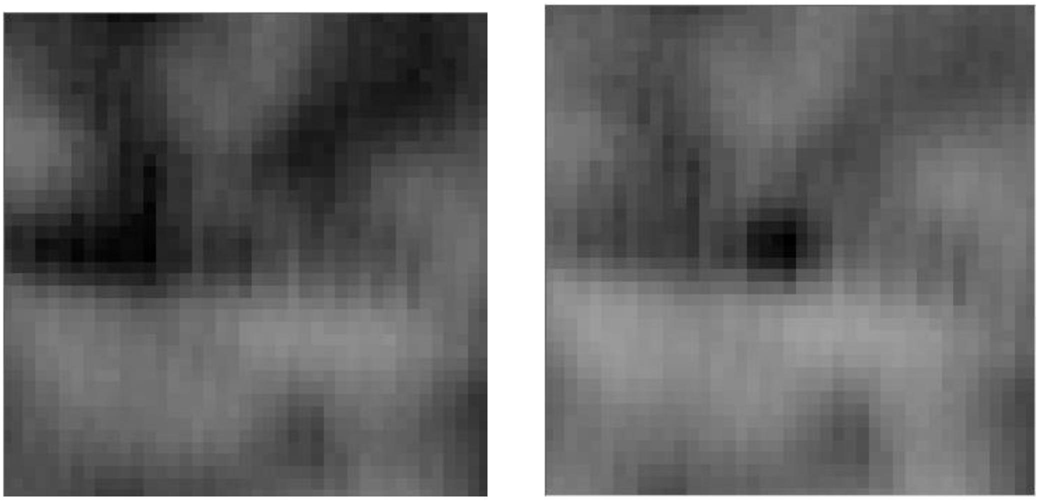

(a) 0.0–1.0 MHz

(b) 0.0–1.2 MHz

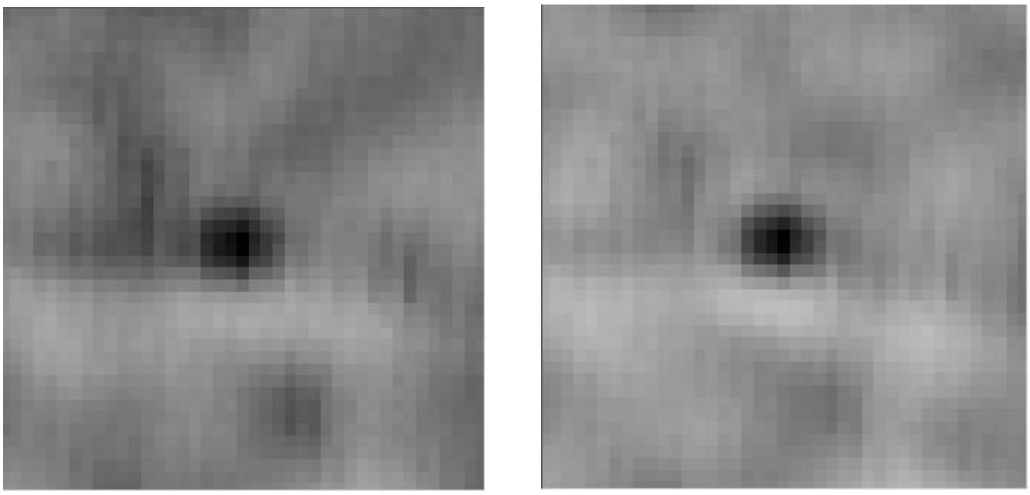

(c) 0.0–1.4 MHz

(d) 0.0–1.6 MHz

Fig. 14 Images of the defect with 0.8 mm diameter with different frequency gates

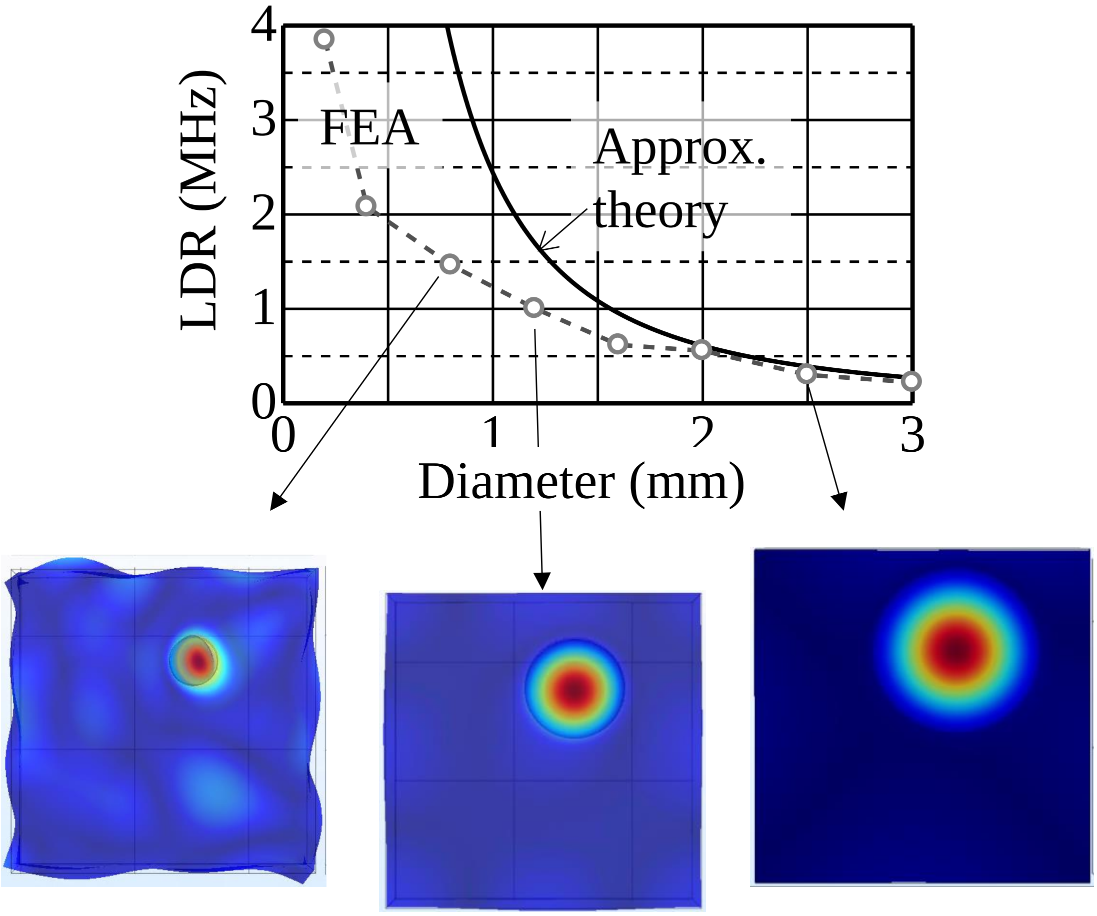

Fig. 15 LDR calculated by Eq. (4) and FEA

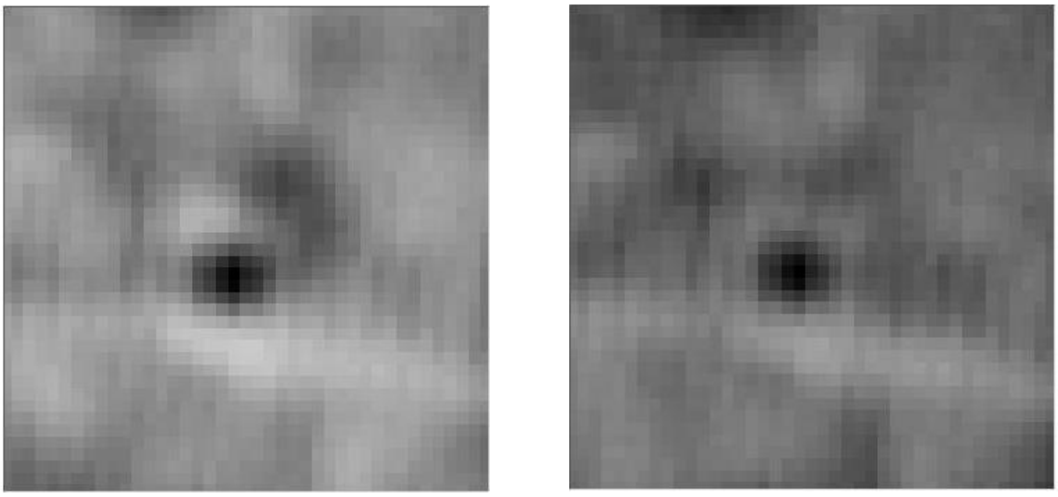

(a) Top surface (b) Back surface

Fig. 16 Images of the 0.8-mm-diameter defect using waveforms detected on the top and back surfaces